# Dynamic analysis and control of mirror segment actuators for the European Extremely Large Telescope

Gert Witvoet
Remco den Breeje
Jan Nijenhuis
René Hazelebach
Niek Doelman

SPIE.

# Dynamic analysis and control of mirror segment actuators for the European Extremely Large Telescope

**Gert Witvoet,\* Remco den Breeje, Jan Nijenhuis, René Hazelebach, and Niek Doelman**
TNO Technical Sciences, Opto-Mechatronics Department, Stieltjesweg 1, 2628 CK Delft, The Netherlands

**Abstract.** Segmented primary mirror telescopes require dedicated piston-tip-tilt actuators for optimal optical performance. Netherlands Organisation for Applied Scientific Research (TNO) has developed various prototypes of such actuators, in particular for the E-ELT. This paper presents the dynamics analysis and feedback control results for a specific two-stage prototype. First, the dynamics of the actuator in interconnection with the to-be-positioned mass has been analyzed, both using frequency response measurements and first principles modeling, resulting in a detailed understanding of the dynamic behavior of the system. Next, feedback controllers for both the fine and the coarse stage have been designed and implemented. Finally, the feedback-controlled actuator has been subjected to a realistic tracking experiment; the achieved results have demonstrated that the TNO actuator is able to suppress wind force disturbances and ground vibrations with more than a factor $10^3$, down to 1.4 nm root mean square, which is compliant with the requirements. © *2015 Society of Photo-Optical Instrumentation Engineers (SPIE)* [DOI: 10.1117/1.JATIS.1.1.019003]

## 1 Introduction

Future extremely large telescopes, such as the Thirty Meter Telescope (TMT), the Giant Magellan Telescope and the European Extremely Large Telescope (E-ELT), will be equipped with segmented primary mirrors (M1). The feasibility of such a segmented M1 concept has successfully been demonstrated on the Keck[1] telescopes; other telescopes with segmented primary mirrors such as the Hobby–Eberly Telescope, the Southern African Large Telescope, and the Gran Telescopio Canarias later followed the Keck example.

To achieve optimal optical performance in such a concept, each individual mirror segment of the M1 should be actively controlled in at least the rigid-body piston-tip-tilt movements. To this extent, each segment can be equipped with three dedicated single-DOF actuators. In case of the E-ELT, the requirements for these piston-tip-tilt actuators, often called position actuator (PACT), are particularly challenging to meet; they should combine ultra-high accuracy with a relatively large stroke, while carrying a large mass in a changing gravitational field and being exposed to nonstationary structural vibrations and wind loads.

Over the last couple of years, Netherlands Organisation for Applied Scientific Research (TNO) has designed and realized various different PACT prototypes for the E-ELT. In 2007, TNO has delivered 18 wind experiment breadboard PACTs[2] to European Southern Observatory (ESO). In the last 2 years, TNO has developed follow-up prototypes which are compliant with updated requirements, regarding e.g., reduced dimensions and power consumption and increased performance. These recent prototypes are intentionally mutually different and vary in several aspects. Each prototype has been extensively tested in a dedicated test setup, and their performance has been assessed in relation to the requirements. As such, experience has been gained with various coarse stage actuators (stepper motor versus brushless DC-motor), spindle types, and lateral supports. Note that a detailed discussion on the prototypes and their differences is outside the scope of this paper.

Instead, this paper considers one of the actuator prototypes (in this case a DC-motor driven PACT with an elastic lateral support) and focuses on the assessment of its dynamics, the subsequent controller design and the resulting performance. Understanding of the overall dynamics, i.e., of the actuator in connection with the load it is required to position, is crucial not only for the PACT controller design, but also for further development of the hardware and *a priori* assessment of the behavior[3,4] and control challenges[5,6] of the complete M1. In this paper, the dynamics of PACT in its M1-relevant test-setup are both measured and modeled, showing a large agreement between the two, which has led to a good comprehension of the overall dynamic behavior. Next, it is shown how a high-performance fine stage controller has been designed based on these dynamics and knowledge of the external disturbances, and combined with a coarse stage controller for off-loading the fine stage. After implementation of these controllers, the actuator performance has been assessed via an E-ELT relevant tracking experiment, in which the assembly of actuator and test mass had to follow a 1.2 $\mu$m/s setpoint in the presence of ground vibrations and (artificial) realistic wind disturbances. It is shown that the resulting root-mean-square (RMS) error is compliant with the 1.7 nm requirement, while the RMS power consumption remains below the required 1 W.

This paper is organized as follows. The hardware comprising the actuator and its test setup will be briefly discussed in Sec. 2. Next, Sec. 3 presents the analysis of the dynamics of the overall system. The subsequent fine and coarse stage controller designs will be described in Sec. 4, which will also present the achieved experimental tracking results. This is followed by the conclusions and some discussion in Sec. 5.

---

*Address all correspondence to: Gert Witvoet, E-mail: Gert.Witvoet@tno.nl

## 2 System Description

In this section, we will first discuss the considered hardware. To this end, the actuator concept and some driving requirements will be summarized, and the test setup in which PACT has been qualified will be described. This information is relevant for the analysis of the dynamics in Sec. 3.
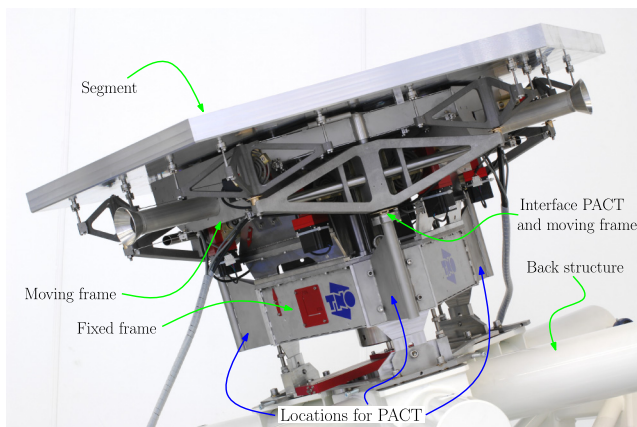
### 2.1 Actuator

The eventual application of PACT is the control of piston, tip, and tilt of M1 segments; three PACTs for a single segment, 798 segments for the whole M1. A specific prototype of an M1 segment support (delivered to ESO in 2010) is shown in Fig. 1, which illustrates the mounting locations of the PACTs and introduces the terminology used in the remainder of this paper. The PACT bodies are foreseen to be mounted on the fixed frame (in this case sideways), while the moving tip of PACT interfaces with the moving frame. As such, three PACTs carry the weight of the complete assembly of the moving frame and the mirror segment.

The requirements for the actuator obviously follow from the M1 application; the recent PACT prototypes developed by TNO have been designed with the following key requirements[7] in mind:

- axial load on an individual actuator: between 0 and 900 N
- orientation: between 0 deg and 90 deg
- PACT should have its own internal metrology
- tracking velocity: up to 1.2 $\mu$m/s
- tracking accuracy: 1.7 nm RMS on the internal metrology
- total stroke: 15 mm
- maximum power dissipation during tracking: less than 1 W
- series production cost price: less than 4000 euro.

To be able to meet the combination of large stroke and high accuracy (note that there is a factor $10^7$ between the two), the PACT prototypes have been designed and realized as two-stage actuators. They are based on a soft actuator principle,[8] i.e., to enable high accuracy a voice coil has been selected for the fine stage. To achieve the 15-mm stroke and to minimize power consumption, this fine stage is off-loaded via a coarse stage spindle



**Fig. 1** Picture of a specific M1 segment support unit prototype, illustrating where the position actuators (PACTs) will be mounted. Photo: TNO/Fred Kamphues.
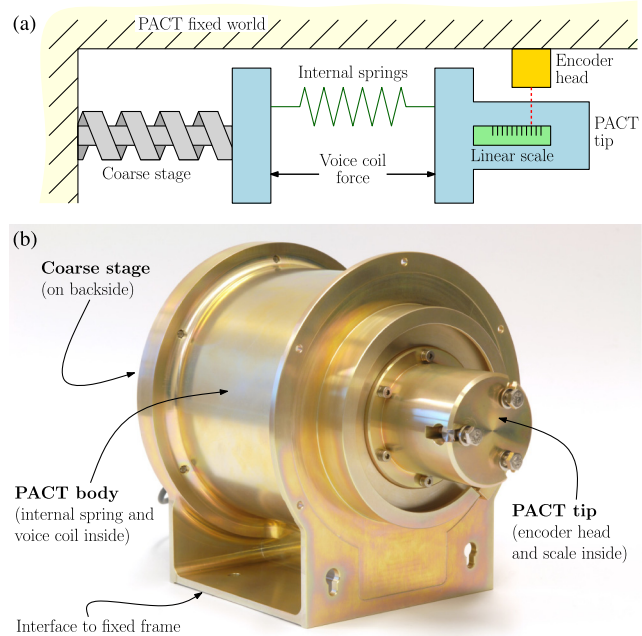


**Fig. 2** Schematic representation of the internals of a single PACT (a), together with a picture of one of the recent prototypes (b). Photo: TNO/ Fred Kamphues.
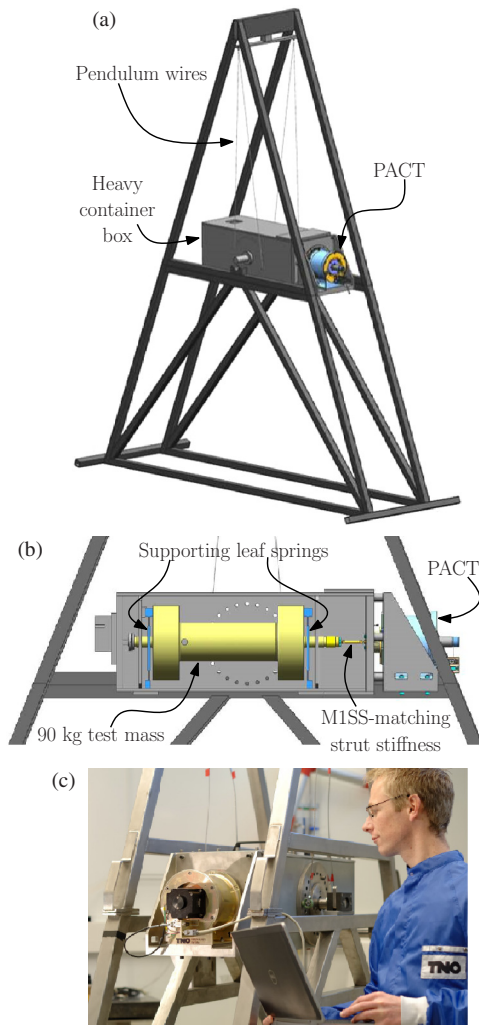
and actuator. Experience has been gained with both a stepper motor and a brushless DC-motor with a gearbox; in this paper only the DC-motor results will be discussed.

As illustrated in the schematic of the PACT internals in Fig. 2(a), the actuator also comprises a set of internal springs, in parallel with the voice coil, to off-load the varying gravity force up to 900 N, which comes with the changing orientation of the mirror segment assembly. Furthermore, to comply with the lateral stiffness requirement, meant to withstand nonaxial loads, PACT is equipped with a lateral support. Each prototype has been made in either of two different embodiments for such a lateral support, as either a sliding bearing or an elastic guidance (leaf spring mechanism); the results in this paper only relate to the PACT with the elastic guidance. Moreover, every PACT prototype has a commercial on-axis nanometer resolution encoder close to the tip of the actuator; this internal metrology will be used as the feedback signal later on. Overall, PACT has been designed with as many commercial off-the-shelf components and easy-to-manufacture parts as possible to keep the cost price low; the aforementioned series production target price is presumably feasible. A picture of one of the TNO prototypes is shown in Fig. 2(b); note that the PACT body interfaces with the fixed frame of an M1 segment support unit (i.e., fixed world), whereas the PACT tip is the moving part of the actuator which interfaces with the moving frame of the same support unit.

### 2.2 Test Setup

To assess the dynamics and performance of a single PACT in relation to the load it is required to actuate, PACT has been mounted in a special M1-relevant test setup. This setup is supposed to mimic the situation that PACT encounters when it is part of an M1 segment support structure assembly. The test setup is visualized in the drawings and picture of Fig. 3. The base of the actuator is mounted to a heavy box (of around 150 kg), which represents the fixed frame of the M1 support

(a)

Pendulum wires

Heavy
container
box

PACT

(b)

Supporting leaf springs

PACT

90 kg test mass

M1SS-matching
strut stiffness

(c)

**Fig. 3** Visualizations of PACT in its test setup; (a) drawing of the complete pendulum assembly; (b) look-in view of the container box, showing the test mass and its guidance (i.e., the leaf springs); (c) picture of the assembly. The actuator displayed in the picture is the one with the stepper motor. Photo: TNO/Fred Kamphues.

structure and a part of the M1 back structure. Inside this box is a 90 kg test mass, guided by some low-stiffness leaf springs, representing the required load which has to be actuated by a single PACT, i.e., a part of the mass of the M1 segment and moving frame. Between this test mass and the actuator is a carefully designed strut which has a stiffness matching the M1 support structure stiffness as experienced by a single PACT.

This complete assembly is hanging on pendulum wires (with relatively low stiffness) so that the box as a whole can freely oscillate. As such, high-frequency ground vibrations are passively attenuated. The reason for this approach is that the ground vibration level in the TNO laboratory where the setup is situated is quite high; by passively attenuating this spectrum a more realistic input disturbance spectrum can be obtained, i.e., more representative for the disturbances present on the E-ELT site. The angle between the box and the horizontal plane, which is labeled $\beta$, can be statically varied (in Fig. 3 the angle is 0 deg). This facilitates doing measurements under various PACT orientations, and thus varying gravitational loads, ranging from fully horizontal (0 N load) to fully vertical (900 N load).

## 3 System Identification

A proper controller design should always start with the identification of the dynamics of the to-be-controlled system. A natural and fast way of doing this is via frequency response function (FRF) measurements.[9] This section will discuss some FRF results, followed by the derivation of a first principles model to explain the observed dynamics.

### 3.1 Frequency Response Measurements

When measuring the frequency response of the overall system (i.e., PACT in its test setup) only the fine stage has been considered, since this is the stage which should eventually meet the accuracy requirement. Proper controller design, in terms of high performance and sufficient robustness, is crucial for this stage and relies heavily on accurate fine stage FRFs.

The FRFs have been obtained in open loop by perturbing the fine stage around various nominal operating points. To this end, the PACT angle $\beta$ and the coarse stage position have been fixed, and then a certain amount of low-pass filtered noise $w$ has been added to the voice coil input, creating a force perturbation on the system. The resulting displacement $y$ of the internal sensor has been measured, so that the local FRF could be calculated from the ratio between the cross-power density $S_{yw}$ and auto-power density $S_{ww}$ of the two signals, i.e.,

$$H_i(j\omega) = \frac{S_{yw}(j\omega)}{S_{ww}(j\omega)}, \tag{1}$$

which is valid around its nominal operating point $i$. By repeating this measurement for different operating points, i.e., for different angles $\beta$ and coarse stage positions, a set of FRFs has been obtained which demonstrates the dependence of the dynamics on the operating point.

The FRF measurements are summarized in Figs. 4 and 5, using 180 s of measurement data per FRF and a resolution of 0.2 Hz. In Fig. 4, the PACT angle is fixed at $\beta = 0$ deg (horizontal position) and the position of the coarse stage is varied over its total stroke of 15 mm. It can be seen that the FRFs are nearly identical, which proves that the fine stage dynamics are hardly dependent on the coarse stage and demonstrate that the actuator behaves linearly over its full stroke. The very minor differences can be allocated to minor changes in the effective mass and stiffness as experienced by the fine stage, since the coarse stage essentially alters the "length" of the actuator. The great resemblance will simplify the controller design and will enable good performance over the complete stroke of the actuator, as will be demonstrated in Sec. 4.

Figure 5 depicts the FRFs as a function of the angle $\beta$, i.e., the angle of the test setup with respect to the horizontal plane, while the position of the coarse stage is fixed at the neutral middle position of 0 mm. Surprisingly, the measurements show that there is a large dependency of the low-frequent eigenmodes on the angle $\beta$. It was realized that this nonlinear effect could have multiple causes; perhaps the dynamics of PACT itself is dependent on the changing gravitational load, or perhaps the test setup in which PACT hangs is intrinsically nonlinear. Since identifying the root cause is impossible by mere observation of the FRF plots, it has been decided to assess the change in dynamic behavior of PACT in connection with a to-be-positioned mass (be it a test mass or an M1 segment) via the derivation of an analytic model based on first principles.
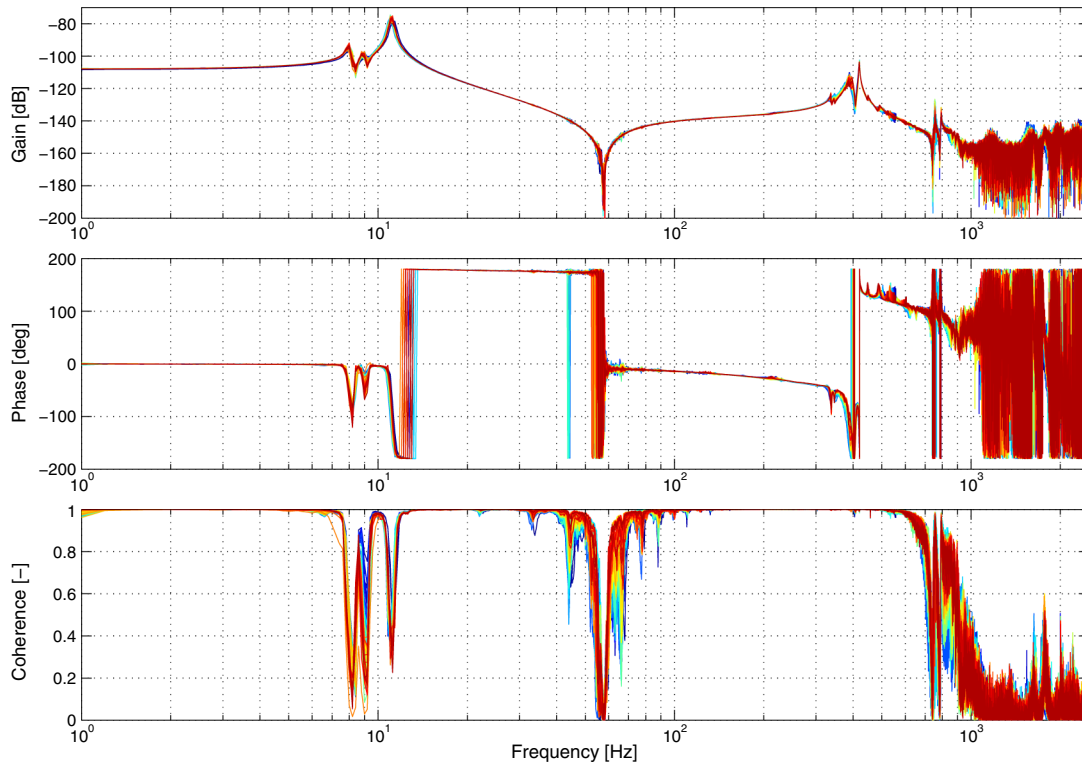
**Fig. 4** Measured frequency response functions (FRFs) of PACT in connection with the test mass, as a function of the coarse stage position (in horizontal configuration); dark blue is fully retracted, dark red is fully extracted.
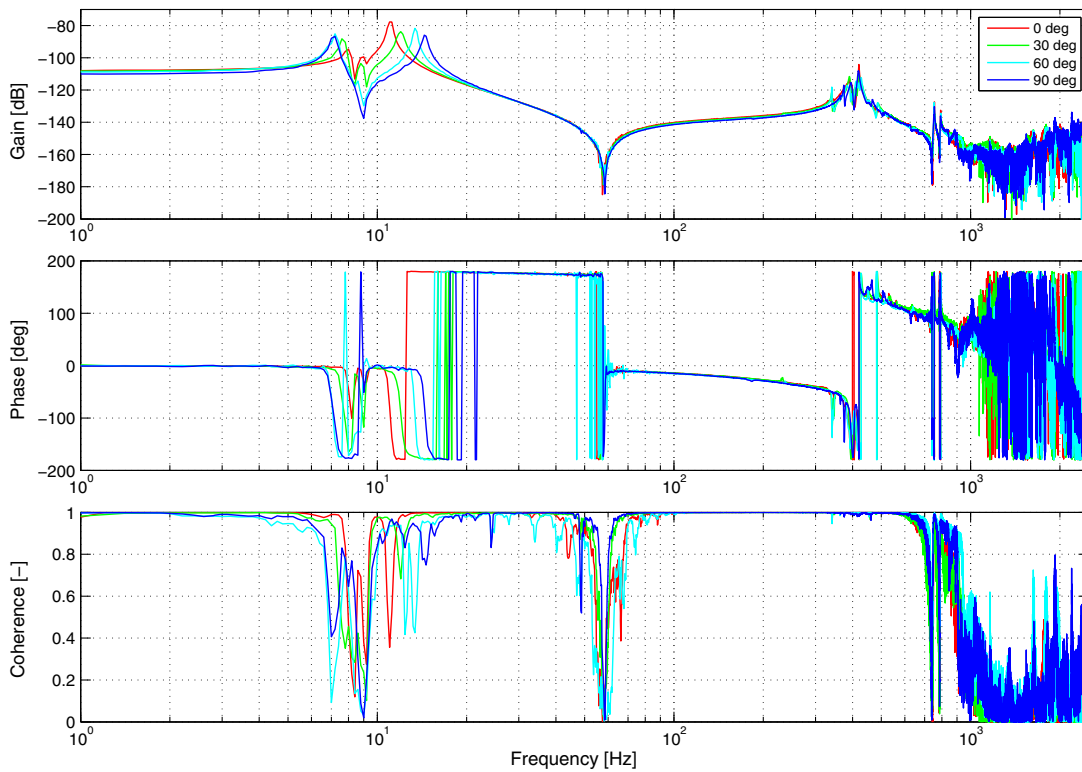


**Fig. 5** Measured FRFs as a function of the angle of PACT with the horizontal plane; note that the low-frequent modes around 10 Hz significantly change.
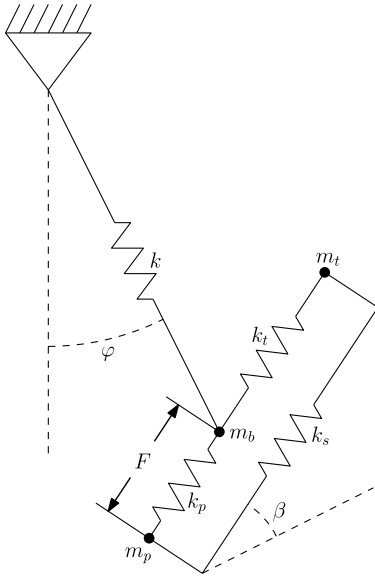
**Fig. 6** Schematic representation of PACT in its test setup.

## 3.2 First Principles Modeling

A schematic representation of the overall system, which forms the starting point for the derivation of the analytic model, is shown in Fig. 6. The model contains three masses, i.e., the moving mass of PACT $m_p$, the test mass $m_t$, and the mass of the surrounding box (including the nonmoving part of PACT) $m_b$. These masses are interconnected via the stiffness of the PACT internal springs $k_p$, a strut stiffness $k_s$ (representing the stiffness of the eventual M1 segment support, as mentioned before), and the stiffness of the linear guidance (leaf springs) of the test mass $k_t$. The box is suspended via the pendulum wire stiffness $k$ to the frame, which in this model represents the fixed world. The nominal length of the pendulum is labeled $L$, while $\delta_p$ and $\delta_t$ denote the off-loaded nominal distance between $m_p$ and $m_b$, and $m_b$ and $m_t$, respectively. The angle $\beta$ which the box makes with respect to the normal of the pendulum is a fixed but tunable parameter; in the test setup $-180 \text{ deg} \leq \beta \leq 180 \text{ deg}$

with steps of 15 deg. The voice coil force $F$ effectively acts between $m_b$ and $m_p$, in parallel to the PACT internal springs $k_p$.

The model has four degrees of freedom (DOF) which can fully describe the motion of the system, namely

$x_p$ : elongation of the PACT springs $k_p$

$x_t$ : elongation of the test mass guidance $k_t$

$y$ : elongation of the pendulum $k$

$\varphi$ : rotation angle of the pendulum.

These generalized DOFs fully define the vertical and horizontal motions of all masses, as shown in Appendix. The equations of motion can be derived using Lagrange's method,[10] which is based on expressions of the kinetic energy $T$, potential energy $V$, and nonconservative forces $Q^{\text{nc}}$:

$$\frac{\mathrm{d}}{\mathrm{d}t}(T_{,\dot{q}}) - T_q + V_{,q} = (Q^{\text{nc}})^T, \tag{2}$$

where $X_{,z}$ denotes the partial derivative of $X$ with respect to $z$ and $q$ is the vector of generalized DOF. The total kinetic energy of the system is defined by the velocity of the masses, i.e.,

$$T = \frac{1}{2}m_b\,v_{\text{box}}^2 + \frac{1}{2}m_p\,v_{\text{PACT}}^2 + \frac{1}{2}m_t\,v_{\text{testmass}}^2, \tag{3}$$

whereas the total potential energy, defined by the springs and the gravitational field, is given by

$$V = \frac{1}{2}ky^2 + \frac{1}{2}k_p x_p^2 + \frac{1}{2}k_t x_t^2 + \frac{1}{2}k_s(x_p - x_t)^2 + m_b g y_{\text{box}}$$
$$+ m_p g y_{\text{PACT}} + m_t g y_{\text{testmass}}. \tag{4}$$

The actuator force $F$ is co-located with $x_p$, so that $Q^{\text{nc}}$ is simply $Q^{\text{nc}} = [F, 0, 0, 0]$. By writing $T$ and $V$ in terms of the generalized DOF, linearizing the expressions around the zero position (i.e., assuming only small rotations $\varphi$), calculating the appropriate partial derivatives, and substituting the results into Eq. (2), we then obtain the undamped equations of motion with mass and stiffness matrices

$$M = \begin{bmatrix} m_p & 0 & -m_p \sin\beta & -m_p L \cos\beta \\ 0 & m_t & -m_t \sin\beta & -m_t L \cos\beta \\ -m_p \sin\beta & -m_t \sin\beta & m_b + m_p + m_t & -(m_p\delta_p - m_t\delta_t)\cos\beta \\ -m_p L \cos\beta & -m_t L \cos\beta & -(m_p\delta_p - m_t\delta_t)\cos\beta & \begin{array}{c}(m_b + m_p + m_t)L^2 \\ +(m_p\delta_p^2 + m_t\delta_t^2) \\ +2\,L(m_p\delta_p - m_t\delta_t)\sin\beta\end{array} \end{bmatrix} \tag{5}$$

$$K = \begin{bmatrix} k_p + k_s & -k_s & 0 & -m_p g \cos\beta \\ -k_s & k_t + k_s & 0 & -m_t g \cos\beta \\ 0 & 0 & k & 0 \\ -m_p g \cos\beta & -m_t g \cos\beta & 0 & \begin{array}{c}(m_b + m_p + m_t)gL \\ +g(m_p\delta_p - m_t\delta_t)\sin\beta\end{array} \end{bmatrix}. \tag{6}$$

More details on the derivation of these matrices can be found in Appendix. The undamped eigenfrequency matrix $\Lambda$ and mode shapes $\Phi$ can be found by solving the eigenvalue problem $K\Phi = M\Phi\Lambda$, with which modal damping can be added to the system. As such, we define

$$D = 2\zeta\sqrt{\Lambda}, \tag{7}$$

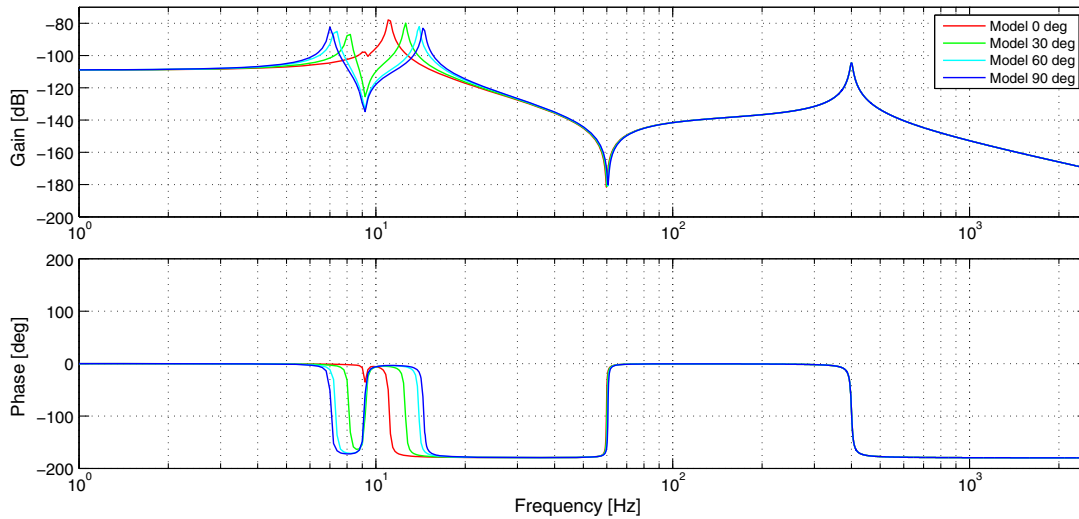where $\zeta$ is the normalized damping ratio. The total model is now given by

**Fig. 7** Frequency responses of the analytic model, as a function of $\beta$.

$$M\ddot{q} + D\dot{q} + Kq = Qu, \tag{8}$$

where the input $u = F$. Moreover, $Q = [1, 0, 0, 0]^T$ and $M$, $D$, and $K$ are as defined in Eqs. (5), (7), and (6), respectively. For control purposes, it is useful to write this model in state-space form, where the system output $z$ is the PACT internal sensor, which in this case corresponds to $x_p$. As such, we obtain

$$\dot{x} = \begin{bmatrix} \mathbf{0} & I \\ -M^{-1}K & -M^{-1}D \end{bmatrix} x + \begin{bmatrix} \mathbf{0} \\ M^{-1}Q \end{bmatrix} u \tag{9}$$

$$z = \begin{bmatrix} 1 & \mathbf{0} \end{bmatrix} x, \tag{10}$$

where $x = [q, \dot{q}]^T$ and $u = F$.

The mass and stiffness parameters of the model have been taken from computer aided design drawings of the actuator and the test setup, and a modal damping of 1% has been assumed for the derivation of $D$. The resulting frequency responses are depicted in Fig. 7, which show a large resemblance to the FRF measurements in Fig. 5. For both, the low-frequent anti-resonance remains steady at 9 Hz for changing $\beta$, while the two surrounding resonances move away from the anti-resonance as $\beta$ increases. Moreover, the model nicely matches the DC-gain, the mass-line between 15 and 50 Hz, the anti-resonance at 60 Hz, and the large resonance around 400 Hz. Hence, the first principles model properly describes the global dynamic behavior, and can be used to assess the mode shapes of the system in general and the $\beta$-dependent low-frequent modes in particular.

### 3.2.1 Mode shape interpretation

Analysis of the computed mode shapes $\Phi$ has revealed that the 60-Hz anti-resonance and 400-Hz resonance correspond to the decoupling of the 90 kg test mass from the moving mass of PACT (1.32 kg). This mode is associated with the strut stiffness $k_s$, and is clearly not influenced by the angle $\beta$. Note that the large ratio between the masses explains why the resonance and anti-resonance are so far apart.

Moreover, there is a pendulum mode of the total mass at 0.47 Hz, which is also not influenced by the angle $\beta$. Since the actuator force solely resides within the heavy box itself, this mode cannot be excited by PACT and is, therefore, uncontrollable, and thus not visible on the FRFs. When $\beta = 0$ deg, the other two modes correspond to the resonance of the total mass on the pendulum wire stiffness $k$ (around 8.7 Hz) and the resonance of the combined masses $m_p$ and $m_t$ with respect to the box $m_b$ on the combined stiffness of $k_p$ and $k_t$ (around 11.1 Hz). For $\beta = 0$ deg, these modes are perpendicular, as the first is a pure radial (or vertical) mode and the second is a pure tangential (or horizontal) one. Consequently, the radial 8.7 Hz mode is nearly unobservable by the internal sensor and is hardly excitable by the voice coil force when PACT is horizontally oriented. However, as $\beta$ increases, the relative displacements of the masses will interact with the radial mode and vice versa. Hence, the stiffnesses $k_p$ and $k_t$ will interact with $k$ in the first resonance, and vice versa in the second. Since $k$ is stiffer than $k_p$ and $k_t$, the eigenfrequency of the first resonance will decrease and that of the second will increase. Moreover, both modes become more observable by the internal sensor and more controllable by the voice coil as $\beta$ increases, and will, therefore, become more visible on the FRFs.

In essence, this analysis has revealed that the stiffness that the masses $m_b$, $m_p$, and $m_t$ "feel" toward the fixed world changes from the one of the swing motion, which is roughly $2 \times 10^3$ N/m, to the one of the pendulum wire $k = 7.2 \times 10^5$ N/m as $\beta$ increases. This is clearly a nonlinear artifact from the test setup itself, and has nothing to do with the actuator. In an assembly with M1 and its support structure this is not likely to occur, since the stiffness to the fixed world in the direction of the actuator is approximately constant in that configuration. As such, we can conclude that the TNO actuator behaves linearly in its complete operational range. Moreover, the above analysis demonstrates the importance of dynamics modeling to understand the behavior of systems and to enable root cause identification.

For the rest of this paper, we will restrict ourselves to the horizontal configuration only. Hence, the FRFs in Fig. 4 will be used in the controller design in Sec. 4.1.

## 3.3 Wind Disturbance Modeling

Apart from having an accurate description of the input–output dynamics of the system, such as presented above, knowledge of the external disturbances in the controller design phase is important to achieve high performance. There are essentially two external disturbances which can limit the performance of a PACT: ground or frame vibrations from below, and wind forces from above.

The exact frame and ground vibrations on the E-ELT site will depend on e.g., the telescope structure and its machinery, but are unknown at the time of writing. However, as the E-ELT will be a seismically isolated very heavy structure in a desolated area, the vibrations will very likely be lower than at the TNO laboratory (second floor in a nonvibration-isolated building in an urban area). This justifies the use of the passive isolation via the test setup pendulum, which brings the vibration spectrum as experienced by PACT in the test setup more into the E-ELT relevant ballpark. Even so, it should be noted that the main focus of this paper is to show how to incorporate specific parts of disturbances (in this case, the TNO laboratory disturbance spectrum) into the controller and to demonstrate the resulting performance improvement, which can be extrapolated to real E-ELT spectra later on.

Wind disturbances will have to be artificially added in a lab environment. To this end, a force disturbance signal is added to the voice coil force. This disturbance signal is generated by filtering a random noise signal such that the output spectrum closely resembles the specified operational spectrum at the E-ELT site.[11] According to these specifications, the on-site wind velocity distribution $S_{uu}(f)$ can be modeled via a von Kármán model[12]

$$S_{uu}(f) = \frac{4I_u^2 V_z L_u}{\left(1 + 70.8\left(\frac{L_u}{V_z}f\right)^2\right)^{5/6}},$$ (11)

where the intensity of turbulence $I_u = 0.4$, the mean wind speed $V_z = 2$ m/s, and the integral length scale of turbulence $L_u = 7$ m. This velocity spectrum can be converted to an approximated force spectrum via the aerodynamic admittance function $\chi_a(f)$ defined as

$$\chi_a(f) = \frac{1}{1 + \left(2f\frac{\sqrt{A}}{V_z}\right)^{4/3}},$$ (12)

where $A = 1.3$ m$^2$ is the area of an M1 segment, and the drag equation is defined as

$$F = \frac{1}{2}\rho V_z^2 A C_d,$$ (13)

where the drag coefficient of a single segment is assumed to be $C_d = 1$ and the mass density of air is assumed to be $\rho = 0.87$ kg/m$^3$ at the E-ELT site.[11] The wind force distribution $S_{FF}(f)$ is then given by[13]

$$S_{FF}(f) = 4\left(\frac{F}{V_z}\right)^2 \chi_a^2(f) \cdot S_{uu}(f).$$ (14)

Using the mentioned parameter values, this yields 1.65 N RMS force on the level of M1, hence a 0.55 N RMS wind force on a single PACT. The corresponding force spectrum, on the level of a single PACT, is shown in Fig. 8. This figure also shows the output spectrum of the fourth-order linear filter (fed by random noise) which is used to simulate this wind spectrum.

Generally speaking, there is a dynamic transmissibility between forces on the surface of an M1 segment and forces on the PACT voice coil. However, it can be shown using, e.g., the analytic model discussed in Sec. 3.2, that this transmissibility is close to unity in the low-frequency range where wind forces are
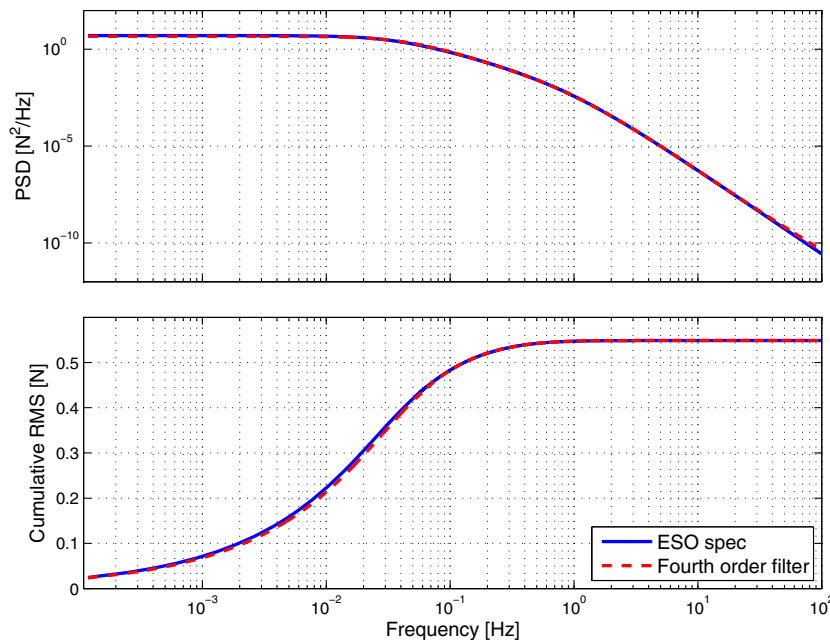


**Fig. 8** Specified wind force disturbance spectrum Eq. (14) on PACT level (solid blue), compared to the output spectrum of the linear filter used to simulate this wind force (dashed red). The bottom plot shows the corresponding cumulative root mean square (RMS).

(a)



(b)
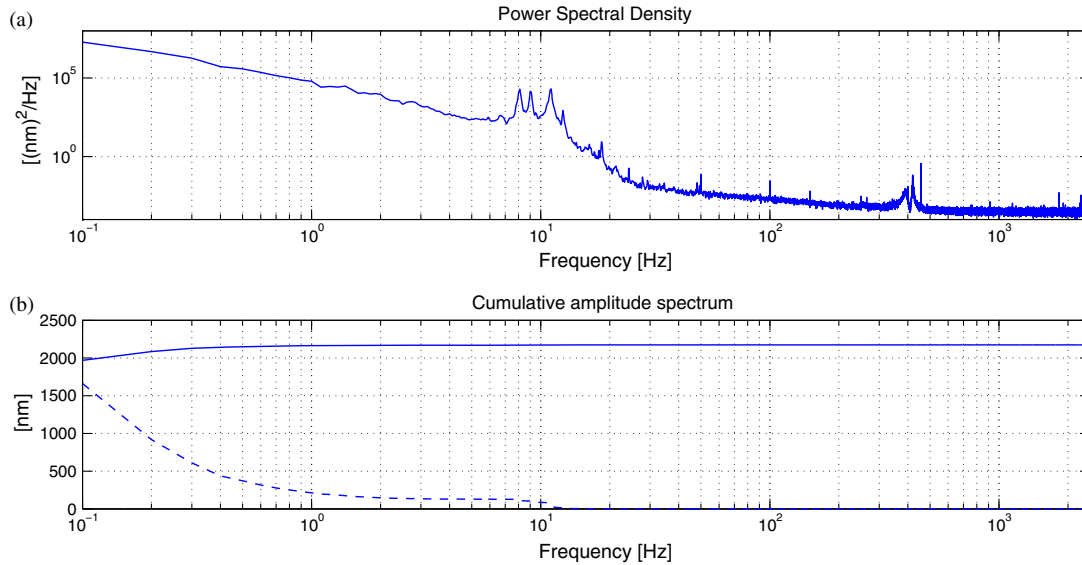


**Fig. 9** Open-loop spectrum of the internal sensor signal in the presence of ground vibrations and wind forces; both the power spectral density (PSD) (a), the left-integrated [(b), solid] and right-integrated cumulative RMS [(b), dashed] are shown.

relevant. Therefore, this transmissibility is neglected in the remainder of this paper.

# 4 Feedback Control

The overall feedback controller design for PACT comprises two parts: one for the fine stage and one for the coarse stage. The fine stage controller design focuses on achieving high performance, whereas the coarse stage controller is merely meant for quasi-static off-loading. The two designs will be treated separately below.

## 4.1 Fine Stage Controller Design

To make proper controller design trade-offs, an open-loop power spectral density (PSD) plot of the error is often very useful. This PSD, as measured by the PACT internal sensor, in the presence of ground and wind disturbances, is shown in Fig. 9. A few aspects of these plots are particularly relevant: the large contribution of wind disturbances below 5 Hz, and the spectral peaks at 8.3, 9.1, and 11 Hz. The open-loop error sums to more than 2 $\mu$m RMS, which should eventually decrease to the required 1.7 nm.[7]

The fine stage controller has been constructed using a loop-shaping design technique. Based on the information in the open-loop PSD, a number of required controller features have been identified which had to be incorporated in this design. Apart from containing a lead filter, which is needed to generate a phase lead in view of closed-loop stability, the controller should

- contain two integrators, to get rid of the low-frequent contribution of the wind forces;

- have a large gain (i.e., contain inverse notches) at 8.3 and 9.1 Hz, to suppress the specifically induced vibrations at these frequencies in closed loop;

- yield a high as possible bandwidth to suppress as many mid-range frequencies as possible;

- contain a low-pass filter, to filter out high-frequency noise sources.

Note that the peak at 11 Hz is not explicitly taken into account in the controller, since it coincides with a resonance in the FRF (see Fig. 4). Consequently, the plant itself already yields a large open-loop gain and resulting closed-loop suppression at that frequency.

Apart from the high-performance target, the controller should also be fairly robust. To this end, a 6 dB-modulus margin[14] is formulated which should hold for all identified FRFs $H_i(j\omega)$ over the coarse stage stroke (see Fig. 4), i.e.,

$$|S_i(j\omega)| = \left| \frac{1}{1 + H_i(j\omega)C(j\omega)} \right| \le 2 \ \forall \ i, \qquad (15)$$

where $C(j\omega)$ is the frequency response of the controller. Note that forcing such a modulus margin implicitly yields minimal phase and gain margins of 29 deg and 6 dB, respectively. Moreover, it has been decided not to completely cancel the 60 Hz anti-resonance by the low-pass filter poles, but to place the latter at a somewhat higher frequency. This way the controller is more robust for changes or uncertainties in this anti-resonance.

After tuning of all its parameters, the controller has been defined as

$$C(s) = 7.19 \times 10^{10} \cdot \underbrace{\frac{\frac{s}{113} + 1}{\frac{s}{1.29 \times 10^3} + 1}}_{\text{lead filter}} \cdot \underbrace{\frac{\frac{s^2}{2.18 \times 10^4} + \frac{s}{369} + 1}{s^2 \left( \frac{s^2}{1.37 \times 10^5} + \frac{s}{1.85 \times 10^5} + 1 \right)}}_{\text{integrators and low-pass filter}} \cdot \underbrace{\frac{\frac{s^2}{2.72 \times 10^3} + \frac{s}{217} + 1}{\frac{s^2}{2.72 \times 10^3} + \frac{s}{2.61 \times 10^4} + 1}}_{\text{notch at 8.3 Hz}} \cdot \underbrace{\frac{\frac{s^2}{3.27 \times 10^3} + \frac{s}{238} + 1}{\frac{s^2}{3.27 \times 10^3} + \frac{s}{2.86 \times 10^4} + 1}}_{\text{notch at 9.1 Hz}}, \qquad (16)$$
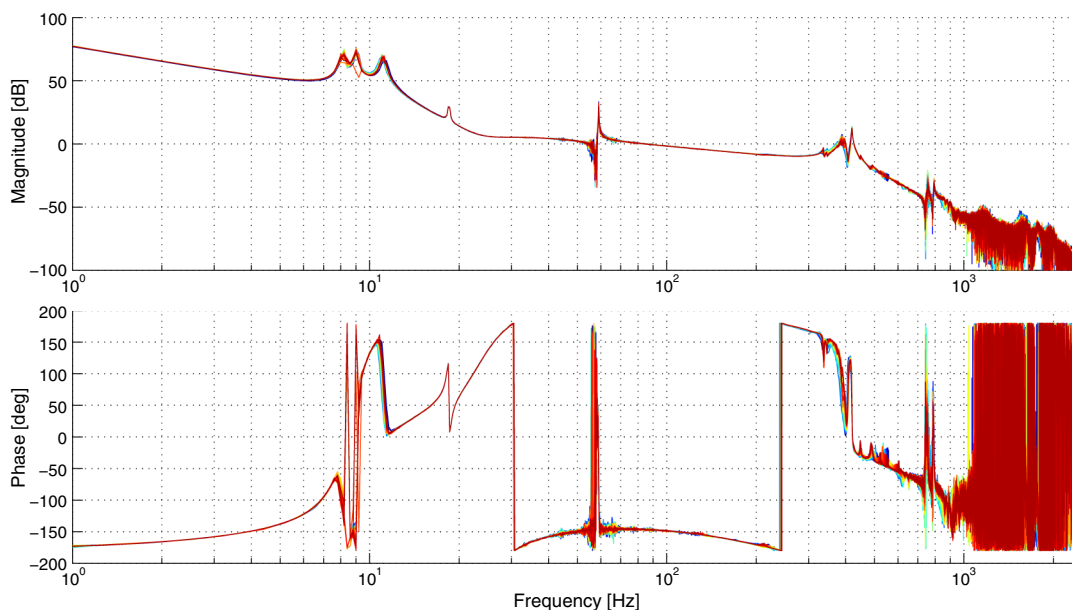
**Fig. 10** Bode diagram of the open-loop frequency response $H_i(j\omega)C(j\omega)$.
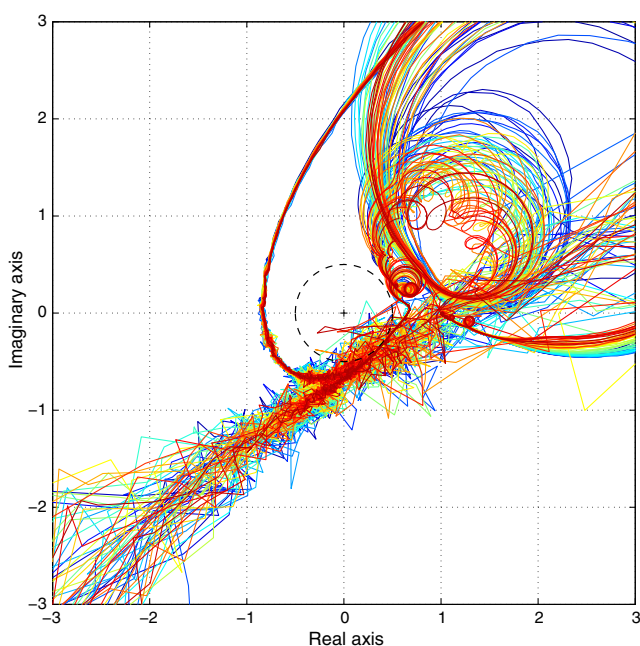


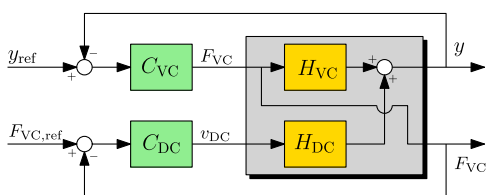**Fig. 11** Nyquist plot of $H_i(j\omega)C(j\omega)$.



**Fig. 12** Block diagram of the combined fine and coarse stage control strategy.

whose frequency-domain performance and robustness are represented in Figs. 10 and 11. These figures show all open loops $H_i(j\omega)C(j\omega)$, both in a Bode plot and in a Nyquist diagram. The former shows that the obtained bandwidth, defined as the 0 dB crossover frequency of the open loop, is roughly between 54 Hz (first crossover) and 85 Hz (second crossover). Note that the open loop slightly peaks through 0 dB again around the 400 Hz mode, hence some closed-loop suppression of this mode can even be expected. The Nyquist plot proves that all loops are indeed closed-loop stable,[14] since the point $(-1, 0)$ is on the left-hand side of all $H_i(j\omega)C(j\omega)$. The robustness is somewhat tricky to judge due to the bad coherence of the FRFs around the 60 Hz anti-resonance; however, looking through the accompanying measurement noise it can be concluded that on average, all $H_i(j\omega)C(j\omega)$ remain outside the dashed disk with radius one-half around the point $(-1, 0)$, which is the graphical representation of the modulus margin. Hence, all loops are considered to satisfy the 6-dB robustness constraint in Eq. (15).

## 4.2 Coarse Stage Controller Design

To demonstrate the tracking performance of PACT over a significant part of the stroke, a coarse stage controller is also needed. This controller has to minimize the power consumption of the voice coil, which is directly linked to the applied voice coil force. To this end, the overall control strategy as illustrated in Fig. 12 has been proposed. The top part of this diagram represents the fine stage loop discussed in Sec. 4.1, where the fine stage controller $C_{VC}$ commands the voice coil actuated plant $H_{VC}$ in order to let the PACT position $y$ track the reference position $y_{ref}$. The accompanying voice coil force $F_{VC}$ is taken as output for the (bottom) coarse stage loop, in which a to-be-designed controller $C_{DC}$ commands a DC-motor velocity $v_{DC}$, affecting the PACT position $y$ and thereby the required voice coil force.

The above approach effectively creates a MIMO (multiple-input-multiple-output) system, which in closed loop can have interaction between its inputs $F_{VC}$ and $v_{DC}$ and outputs $y$ and $F_{VC}$. This can be dealt with by using a sequential loop closing[14,15]
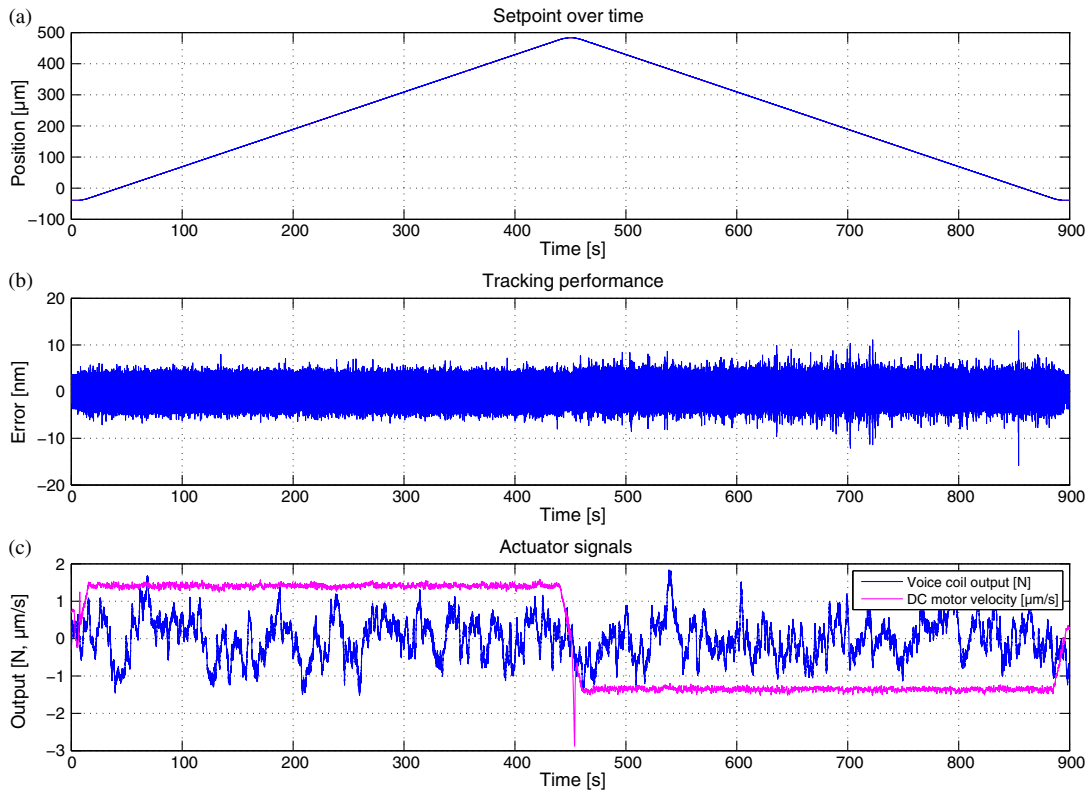
**Fig. 13** Measured closed-loop tracking results: setpoint and output (a), tracking error (b) and voice coil force and DC-motor velocity (c).

approach. First, the high-bandwidth fine stage loop has been closed, as discussed in Sec. 4.1, so that the resulting equivalent plant $H_{eq}$ for the coarse stage controller can be determined as

$$H_{eq} = -\frac{C_{VC}}{1 + C_{VC}H_{VC}} \cdot H_{DC}. \tag{17}$$

The plant $H_{DC}$ actually represents a local velocity control loop of the DC-motor. This local controller operates on the

torque of the DC-motor with a fairly high bandwidth, so that the real velocity is equal to the reference value $v_{DC}$ up to a certain frequency. As such, this velocity controller has a linearizing effect, since it removes the effect of dry and viscous friction in the DC-motor and accompanying gearbox to a large extent. As a result, $H_{DC}$, denoting the transfer function from the velocity $v_{DC}$ to the position $y$, behaves like a simple integrator for low frequencies. Since $C_{VC}/(1 + C_{VC}H_{VC})$ is nearly constant for low frequencies, the same holds for the equivalent plant
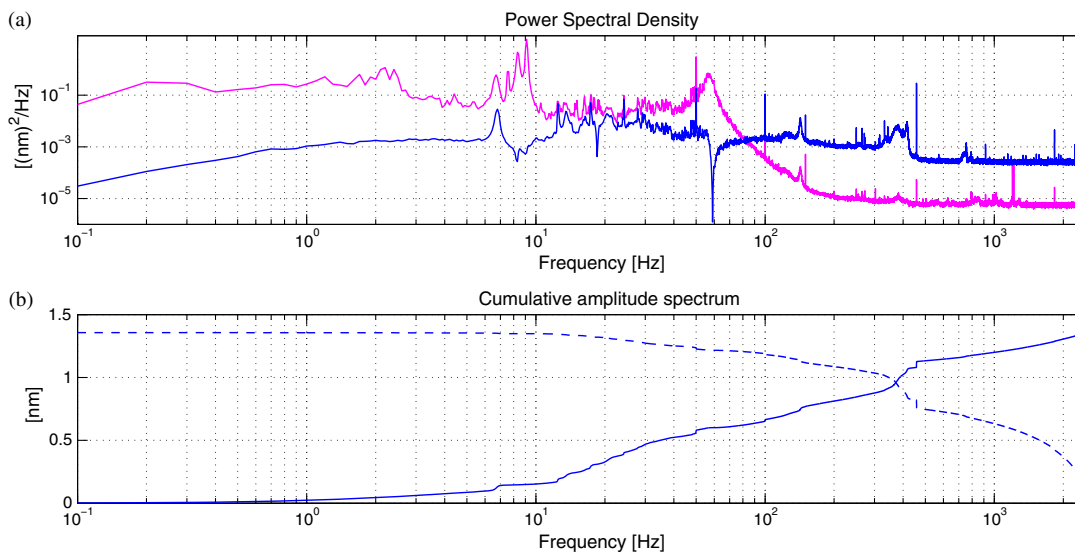


**Fig. 14** Frequency domain representation of the measured error: PSD of the error signal [(a), blue], and its left- [(b), solid] and right-integrated [(b), dashed] cumulative RMS. The top plot also shows the PSD of the interferometric reference data (magenta).
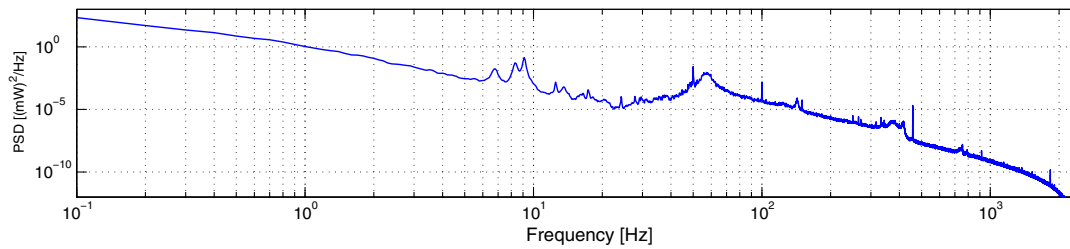
**Fig. 15** Power spectral density of the consumed voice coil power.

$H_{eq}$; in other words, a constant $v_{DC}$ will result in a linearly increasing $F_{VC}$.

In the second loop closing step, a low-bandwidth controller $C_{DC}$ for this $H_{eq}$ has been tuned. In this case, the coarse stage is mainly meant for low-frequent off-loading of the voice coil, hence $C_{DC}$ can simply be a gain with a 2 Hz-low-pass filter, resulting in a bandwidth well below 1 Hz. The large separation in bandwidths of the fine and coarse stage, together with the fact that the MIMO plant actually has a triangular structure (i.e., there is no open-loop transfer between $v_{DC}$ and $F_{VC}$), justifies the use of sequential loop closing. In that case, interaction of the two loops is minimized and MIMO stability can be guaranteed.[14]

### 4.3 Closed-Loop Tracking Results

To demonstrate the performance of the actuator, the above discussed fine and coarse stage controllers have been implemented and applied to PACT (mounted in its test setup, in horizontal configuration). While in closed loop, the actuator has been subjected to an E-ELT relevant scenario. To this end, the position setpoint is initially constant, then gradually increased to a constant tracking velocity[7] of 1.2 $\mu$m/s, and then reversed with the same velocity in the opposite direction. This motion cycle lasts 900 s, thereby covering more than a 500 $\mu$m stroke. The resulting closed-loop response as measured by the internal metrology, both in time and frequency domains, is depicted in Figs. 13 and 14.

The time domain plot in Fig. 13 shows that the setpoint is accurately tracked within $\pm 10$ nm. The error is slightly larger in the backward "downhill" motion than in the forward "uphill" motion, which can be attributed to the self-locking behavior of the coarse stage. During a "downhill" motion the actuator is pulling its moving mass out of self-locked positions into the gearbox play, resulting in small stick-slip-like behavior. However, the impact of this on the fine stage performance is very small. The voice coil force in the bottom plot of Fig. 13 clearly shows the compensation of the low-frequent wind disturbances. Still, this force nicely oscillates around zero, well within $\pm 2$N, due to the DC-motor off-loading with nearly constant velocity. Note that this DC-motor velocity is somewhat larger than the requested 1.2$\mu$m/s; the coarse stage partly pushes against the PACT stiffness $k_p$, so that the effective displacement is somewhat smaller than the coarse stage has moved.

The frequency domain representation of the measured error, depicted in Fig. 14, shows that the RMS error is only 1.4 nm, i.e., well within the requirement. This is roughly a factor 1.5 × $10^3$ improvement compared to the open loop response. The PSD shows that the low-frequent wind contribution, the vibrations at 8.3 and 9.1 Hz and the resonance at 11 Hz are indeed very well suppressed. Some other peaks still remain, but the cumulative spectra prove that these peaks do not significantly contribute

to the total RMS error; hence, it has been decided not to further improve the controller design. It is estimated that at least 0.5 nm of the obtained 1.4 nm can be attributed to sensor noise.

Figure 14 also shows the PSD of a simultaneous subnanometer resolution interferometric reference sensor, which measures $x_t$, i.e., the relative motion between the test mass and the box. Since the PACT internal encoder measures $x_p$, the two sensor measurements are not exactly alike, in the sense that there are dynamics between $x_p$ and $x_t$. This gives rise to a broad peak in the PSD of the interferometer around 60 Hz. Moreover, the 8.3 and 9.1 Hz vibrations are still noticeable between the box and test mass, although they are fully suppressed at the PACT encoder. Even so, the interferometer PSD sums to just 3.4 nm RMS of the test mass motion; this essentially justifies the use of the feedback-controlled internal sensor as a measure for the PACT performance.

From the information in the bottom plot of Fig. 13, we can make an estimate of the power consumption of the actuator. Using the motor constant of the voice coil, which is 7.92 N/W$^{1/2}$, the voice coil force can be converted into power, yielding an instantaneous peak power of 54 mW. The PSD of this power is depicted in Fig. 15, showing specific voice coil effort at e.g., the 8.3 and 9.1 Hz vibrations, around the bandwidth region and even around the 400 Hz mode. The PSD integrates to an RMS value of only 7.6 mW. Due to the large gearbox ratio of the coarse stage, the power consumption of the DC-motor is even smaller and can be neglected. The largest consumer of the power budget is the internal sensor, which uses a total of 0.95 W. Overall, PACT thus consumes less than 0.96 W RMS, which is just within the 1 W requirement.

## 5 Conclusions

TNO has designed and realized various piston-tip-tilt actuator prototypes for the segmented primary mirror of large telescopes, in particular for the E-ELT. This paper has presented some recently obtained control results with one of these prototypes. To this end, frequency response measurements have been taken and a first principles model of PACT in interaction with its test setup has been derived, with which the dynamics of the actuator have been assessed and successfully understood. Next, based on the measured dynamics and knowledge of the external disturbances, a high-performance fine stage controller has been designed, using the PACT internal metrology as feedback sensor, and a low-bandwidth coarse stage controller has been derived for fine stage off-loading purposes. Finally, an E-ELT relevant tracking experiment has been presented, which has demonstrated the high performance of the feedback-controlled PACT. A position error of just 1.4 nm RMS has been obtained, even in the presence of both ground vibrations and wind disturbances, while the RMS power consumption is just 0.96 W.

This result is clearly compliant with the requirements, but it should be noted that the 1.7 nm accuracy requirement is specified at the level of PACT itself, being a relative measure between the fixed frame of the segment support and the PACT tip. This does not automatically imply the same positioning accuracy at the M1 segment level. There are a significant amount of dynamics between PACT and the M1 segment surface, which can be excited even though the actuator is standing still. The decoupling of the M1 mass $m_t$ with respect to the PACT moving mass $m_p$ around the support structure stiffness $k_s$, associated with the 60 Hz anti-resonance and 400 Hz resonance, is particularly relevant in this regard. But higher order modes will also cause the segment to move relative to PACT, especially when looking at nanometer scales.

Considering the aforementioned, the M1 segment positioning relative to the fixed frame could potentially be improved by a modified controller design, most likely at the expense of a worse performance at the PACT level. However, this still does not guarantee a good absolute positioning of a segment, i.e., relative to the sky, or a good co-phasing of adjacent segments. In the current baseline control approach, any PACT closed loop will create a stiff connection between an M1 segment and the fixed frame; this is obviously beneficial for wind force attenuation, but frame vibrations are directly transferred to the segment. As such, segments will vibrate with respect to the sky, and adjacent segments could possibly vibrate with respect to each other if the spatial content of the frame vibrations is not sufficiently low (note that the edge sensor loops are specified to run at a 1 Hz bandwidth, whereas frame vibrations are typically at much higher frequencies). For this reason, TNO is also investigating alternative control approaches, such as acceleration feedback,[16] the use of force sensors, Kalman filtering, or inferential control. Apart from this, TNO continues to evaluate the different PACT prototypes, and aims to provide the best possible position actuator, with accompanying control strategies, for segmented primary mirror telescopes.

## Appendix: Further Modeling Details

As mentioned in Sec. 3.2, all horizontal and vertical movements of the masses of the model represented in Fig. 6 can be expressed in terms of the generalized DOF $q = [x_p, x_t, y, \varphi]^T$. Assuming only small angles $\varphi$ and displacements $y$, $x_p$, and $x_t$, these expressions can be approximated by

$$\text{Box:}\begin{cases} \text{Hor:} & (L - y) \sin \varphi & \approx L\varphi \\ \text{Ver:} & L - (L - y) \cos \varphi & \approx y \end{cases} \tag{18}$$

$$\text{PACT:}\begin{cases} \text{Hor:} & (L - y) \sin \varphi - (\delta_p + x_p) \cos(\beta + \varphi) & \approx L\varphi + \delta_p\varphi \sin \beta - x_p \cos \beta \\ \text{Ver:} & L - (L - y) \cos \varphi - (\delta_p + x_p) \sin(\beta + \varphi) & \approx y - \delta_p\varphi \cos \beta - x_p \sin \beta \end{cases} \tag{19}$$

$$\text{Test mass:}\begin{cases} \text{Hor:} & (L - y) \sin \varphi + (\delta_t - x_t) \cos(\beta + \varphi) & \approx L\varphi - \delta_t\varphi \sin \beta - x_t \cos \beta \\ \text{Ver:} & L - (L - y) \cos \varphi + (\delta_t - x_t) \sin(\beta + \varphi) & \approx y + \delta_t\varphi \cos \beta - x_t \sin \beta \end{cases} \tag{20}$$

These expressions can then be used to derive the kinetic energy $T$, potential energy $V$, and their partial derivatives for substitution in the Lagrange Eq. (2). Hence, Eq. (3) elaborates to

$$T \approx \frac{1}{2}(m_b + m_p + m_t)(L^2\dot{\varphi}^2 + \dot{y}^2) + \frac{1}{2}m_p[\delta_p^2\dot{\varphi}^2 + \dot{x}_p^2 + 2 L\dot{\varphi}^2\delta_p \sin \beta - 2 L\dot{\varphi}\dot{x}_p \cos \beta - 2\dot{y} \dot{\varphi} \delta_p \cos \beta - 2\dot{y}\dot{x}_p \sin \beta]$$
$$+ \frac{1}{2}m_t[\delta_t^2\dot{\varphi}^2 + \dot{x}_t^2 - 2 L\dot{\varphi}^2\delta_t \sin \beta - 2 L\dot{\varphi}\dot{x}_t \cos \beta + 2\dot{y} \dot{\varphi} \delta_t \cos \beta - 2\dot{y}\dot{x}_t \sin \beta], \tag{21}$$

so that its derivatives become

$$\frac{\mathrm{d}}{\mathrm{d}t}(T_{,\dot{q}}) = \begin{bmatrix} m_p\ddot{x}_p - m_pL\ddot{\varphi} \cos \beta - m_p\ddot{y} \sin \beta \\ m_t\ddot{x}_t - m_tL\ddot{\varphi} \cos \beta - m_t\ddot{y} \sin \beta \\ (m_b + m_p + m_t)\ddot{y} - m_p\delta_p\ddot{\varphi} \cos \beta - m_p\ddot{x}_p \sin \beta + m_t\delta_t\ddot{\varphi} \cos \beta - m_t\ddot{x}_t \sin \beta \\ (m_b + m_p + m_t)L^2\ddot{\varphi} + (m_p\delta_p^2 + m_t\delta_t^2)\ddot{\varphi} + 2 L(m_p\delta_p - m_t\delta_t)\ddot{\varphi} \sin \beta \\ - m_pL\ddot{x}_p \cos \beta - m_tL\ddot{x}_t \cos \beta - \ddot{y}(m_p\delta_p - m_t\delta_t) \cos \beta \end{bmatrix} \tag{22}$$

$$T_{,q} = \begin{bmatrix} 0 & 0 & 0 & 0 \end{bmatrix}^T \tag{23}$$

Similarly, Eq. (4) elaborates to

$$V = \frac{1}{2}ky^2 + \frac{1}{2}k_px_p^2 + \frac{1}{2}k_tx_t^2 + \frac{1}{2}k_s(x_p - x_t)^2 + (m_b + m_p + m_t)g[L(1 - \cos \varphi) + y \cos \varphi] - m_pg(\delta_p + x_p) \sin(\beta + \varphi)$$
$$+ m_tg(\delta_t - x_t) \sin(\beta + \varphi), \tag{24}$$

so that its derivative can be approximated by

$$V_{,q} \approx \begin{bmatrix} (k_p + k_s)x_p + k_s x_t - m_p g\varphi \cos \beta \\ (k_t + k_s)x_t + k_s x_p - m_t g\varphi \cos \beta \\ ky \\ (m_b + m_p + m_t)gL\varphi + g\varphi(m_p\delta_p - m_t\delta_t) \sin \beta - m_p g x_p \cos \beta - m_t g x_t \cos \beta \end{bmatrix}. \tag{25}$$

Substitution of the Eqs. (22), (23), (25) and the nonconservative forces $Q^{nc} = [F, 0, 0, 0]$ into Eq. (2) then yields the equations of motion for the complete setup, i.e.,

$$m_p\ddot{x}_p - m_p L\ddot{\varphi} \cos \beta - m_p\ddot{y} \sin \beta + (k_p + k_s)x_p$$
$$- k_s x_t - m_p g\varphi \cos \beta = F \tag{26}$$

$$m_t\ddot{x}_t - m_t L\ddot{\varphi} \cos \beta - m_t\ddot{y} \sin \beta + (k_t + k_s)x_t$$
$$- k_s x_p - m_t g\varphi \cos \beta = 0 \tag{27}$$

$$(m_b + m_p + m_t)\ddot{y} - m_p\delta_p\ddot{\varphi} \cos \beta - m_p\ddot{x}_p \sin \beta$$
$$+ m_t\delta_t\ddot{\varphi} \cos \beta - m_t\ddot{x}_t \sin \beta + ky = 0 \tag{28}$$

$$(m_b + m_p + m_t)L^2\ddot{\varphi} + (m_p\delta_p^2 + m_t\delta_t^2)\ddot{\varphi}$$
$$+ 2 L(m_p\delta_p - m_t\delta_t)\ddot{\varphi} \sin \beta$$
$$- m_p L\ddot{x}_p \cos \beta - m_t L\ddot{x}_t \cos \beta - \ddot{y}(m_p\delta_p - m_t\delta_t) \cos \beta$$
$$+ (m_b + m_p + m_t)gL\varphi + g\varphi(m_p\delta_p - m_t\delta_t) \sin \beta$$
$$- m_p g x_p \cos \beta - m_t g x_t \cos \beta = 0. \tag{29}$$

Since these equations are linear in the generalized DOF $q$ and its derivatives, they can be written in the matrix form of Eq. (8) (with $D = 0$), from which the matrices $M$ and $K$ as defined in Eqs. (5) and (6) follow automatically.

## References

1. R. C. Jared et al., "The W.M. Keck telescope segmented primary mirror active control system," *Proc. SPIE* **1236**, 996–1008 (1990).
2. F. Kamphues et al., "PACT: the actuator to support the primary mirror of the ELT," *Proc. SPIE* **7018**, 70180Z (2008).
3. B. Sedghi, M. Müller, and B. Bauvir, "Dynamical simulation of E-ELT segmented primary mirror," *Proc. SPIE* **8336**, 83360D (2011).
4. M. W. Regehr et al., "Dynamic characterization of a prototype of the thirty meter telescope primary segment assembly," *Proc. SPIE* **7733**, 77332G (2010).
5. P. M. Thompson, D. G. MacMynowski, and M. J. Sirota, "Control analysis of the TMT primary segment assembly," *Proc. SPIE* **7012**, 70121N (2008).
6. M. Dimmler et al., "E-ELT primary mirror control system," *Proc. SPIE* **7012**, 70121O (2008).
7. T. Erm, "Technical specification for the manufacturing and delivery of prototype position actuators for the primary mirror of the European extremely large telescope (E-ELT)," E-SPE-ESO-142-0011 Technical Report issue 2, ESO (2009).
8. P. M. Thompson et al., "Servo design and analysis for the Thirty Meter Telescope primary mirror actuators," *Proc. SPIE* **7733**, 77332F (2010).
9. R. Pintelon and J. Schoukens, *System Identification: A Frequency Domain Approach*, Wiley-IEEE Press, Piscataway, New Jersey (2004).
10. A. de Kraker, *Mechanical Vibrations*, Shaker Publishing, Maastricht, The Netherlands (2009).
11. B. Koehler, "E-ELT environmental conditions," E-SPE-ESO-313-0111 Technical Report issue 5, ESO (2012).
12. ESDU 85020, *Characteristics of Atmospheric Turbulence Near the Ground. Part II: Single Point Data for Strong Winds*, Engineering Sciences Data Unit, London, United Kingdom (1985).
13. G. Tomasini and F. Cheli, "Admittance function to evaluate aerodynamic loads on vehicles: experimental data and numerical model," *J. Fluids Struct.* **38**, 92–106 (2013).
14. S. Skogestad and I. Postlethwaite, *Multivariable Feedback Control: Analysis and Design*, John Wiley, Chichester, United Kingdom (2005).
15. M. Hovd and S. Skogestad, "Sequential design of decentralized controllers," *Automatica* **30**(10), 1601–1607 (1994).
16. B. Sedghi, B. Bauvir, and M. Dimmler, "Acceleration feedback control on an AT," *Proc. SPIE* **7012**, 70121Q (2008).

**Gert Witvoet** is a control specialist at TNO Technical Sciences. He received his MSc (cum laude) and PhD degrees in mechanical engineering, specializing in control engineering, from Eindhoven University of Technology in 2007 and 2011, respectively. His current research interests include dynamical modeling and analysis, opto-mechatronic systems and (advanced) control engineering, for space, astronomy, and nuclear fusion applications. He is also a lecturer on motion control at Eindhoven University of Technology.

**Remco den Breeje** received his BSc degree in applied physics from the The Hague University of Applied Sciences in 2005. At TNO, he has gained many years of experience in various semiconductor and astronomy projects, working as electronics, mechatronics, and control engineer. He is specialized in real-time control platforms and algorithms; specific application domains including adaptive optics, mechatronics, and space instruments.

**Jan Nijenhuis** has worked as system engineer at TNO Technical Sciences. In 1980, he graduated (cum laude) at Delft University of Technology in structural engineering and design. Eight years later, he led the design of the flight controls of the Fokker aircraft. Since 1998, he has specialized in the design of opto-mechanical systems, for which he received the Rien Koster award from the Dutch Society for Precision Engineering in 2008.

**René Hazelebach** is a mechanical design engineer at TNO Technical Sciences. He received his BSc degree in precision engineering from the University of Applied Sciences Utrecht/Hilversum in 1988. He is currently involved in various space, astronomical, and semiconductor projects.

**Niek Doelman** received his MSc (cum laude) and PhD degrees in applied physics from Delft University of Technology in 1987 and 1993, respectively. He is a senior scientist at TNO and since 2012 a part-time professor at the Leiden Observatory with research chair "Control for Astronomy Instruments." His main research interests include active and adaptive optics, vibration control and mechatronics for the space, lithography, astronomy, medical instruments, and nuclear fusion application fields.